WATER VAPOR AND AEROSOLS FROM CHEMCAM PASSIVE SKY OBSERVATIONS

T. H. McConnochie, *Department of Astronomy, University of Maryland, College Park, MD, United States and NASA Goddard Space Flight Center, Greenbelt, MD, United States (tmcconno@umd.edu)*, **M. D. Smith,** *NASA Goddard Space Flight Center, Greenbelt, MD, United States,* **M. J. Wolff**, *Space Science Institute, Boulder, CO, United States*, **S. Bender**, *Planetary Science Institute, Tucson, AZ, United States*, **M. Lemmon**, *Texas A&M University, College Station, TX, United States*, **R. C. Wiens**, *Los Alamos National Laboratory, Los Alamos, NM, USA*, **S. Maurice**, **O. Gasnault**, **J. Lasue**, **P.-Y. Meslin**, *Institut de Recherche en Astrophysique et Planetologie, Toulouse, France*, **A.-M. Harri**, **M. Genzer**, *Finnish Meteorological Institute, Helsinki, Finland*, **O. Kemppinen**, *Finnish Meteorological Institute, Helsinki, Finland and Kansas State University, Manhattan, KS, United States*, **G. M. Martínez**, *Department of Climate and Space Sciences and Engineering, University of Michigan, Ann Arbor, MI, USA*, **L. DeFlores**, **D. Blaney**, *Jet Propulsion Laboratory, Pasadena, CA, United States*, **J. R. Johnson**, *Johns Hopkins University Applied Physics Laboratory, Laurel, MD, United States*, **J. F. Bell III**, *Arizona State University, Tempe, AZ, United States*.

Introduction: The Mars Science Laboratory's (MSL) ChemCam spectrometer [1, 2] measures atmospheric aerosol properties and gas abundances by operating in passive mode and observing scattered sky light at two different elevation angles. ChemCam was designed primarily for laser induced breakdown spectroscopy (LIBS) of Martian surface materials [3,4] but it has been used extensively for both imaging [5] and passive spectroscopy [6]. Here we discuss the methodology and initial results of ChemCam passive sky spectroscopy with ChemCam's VNIR (visible and near infrared) spectrometer. We focus on water vapor abundances, but we also provide preliminary results for aerosols. We retrieve molecular oxygen as well from ChemCam passive sky observations [7, 8], but our data analysis for O_2 remains a work in progress and so we will not report those results here.

The ChemCam data set that we present here extends from MY 31 L_s = 291° to MY 33 L_s=127°, covering data available in the Planetary Data System as of October 2016. In this period 113 passive sky observations pass our quality controls.

Methodology: By observing at two different elevation angles we collect scattered skylight that has traced two significantly different path lengths through the atmosphere, and by ratioing the low elevation signal to the high elevation signal we eliminate solar spectral features and instrument response uncertainties. Using a discrete-ordinates multiple-scattering radiative transfer model, we fit the continuum of the ratio to solve for aerosol properties and then the continuum-removed ratio to solve for gas abundances.

We fit the continuum at 15 evenly spaced wavelengths ranging from 550 to 830 nm. The aerosol property parameters used to fit the continuum ratio are dust particle effective radius, ice particle effective radius, and the fraction of 880 nm opacity contributed by dust, with the total 880 nm opacity constrained by Mastcam direct-sun imaging. (Since Mastcam measures opacity in a narrow-band filter centered at 880 nm, we use 880 nm as the reference wavelength for expressing all opacities even though ChemCam is not sensitive to this particular wavelength.) The gas abundances used to fit the continuum-removed ratio are O_2 volume mixing ratio based on the O_2 "A" band near 762 nm, CO_2 volume mixing ratio based on bands near 783 nm and 789 nm, and water vapor column in precipitable microns based on line groups in the 719 – 730 nm and 810 – 835 nm ranges. We treat all gasses as uniformly vertically mixed in our standard retrievals.

In the final stages of our retrieval we iteratively adjust an aerosol extinction scale height parameter (expressed as gas scale height over dust or ice extinction scale height) and repeat the gas abundance fit to find the unique parametric relationship between CO_2 abundance and the other gas abundances. We use this to correct water vapor abundances, and also to estimate the aerosol extinction scale height, based on the known [9] correct value for CO_2 (96.0%). For the results that we present here, we base the corrections for water vapor on a 20°-of-solar-longitude-wide moving average of apparent CO_2 abundances. We find that using the moving average of CO_2 reduces the scatter in water vapor results in some time periods while having only negligible effects in high-data-quality periods.

After completing all retrievals we use the fit-residual covariance matrices calculated from the complete set of retrievals to make a Monte-Carlo estimate of the gas abundance uncertainties of each retrieval. The CO_2 fit residuals determine the uncertainty estimate for the aerosol scale height parameter. In addition they contribute to the final uncertainty estimate for both O_2 and water vapor because of the correction procedure described in the previous paragraph. For the remaining aerosol parameters, the statistical instrumental uncertainties are negligible compared to the effects of systematic errors and uncertain inputs.

Water Vapor Results: Our initial results give water vapor column abundances with a precision of +/- 0.6 precipitable microns. Sensitivity tests and analysis of water vapor results indicates that systematic errors are no larger than +/- 0.3 precipitable microns, except for the effects of deviations from the assumed uniformly-mixed vertical profile. For extreme cases, which are only plausible for the northern summer season, a condensation-level-limited vertical profile could cause our results to be positively biased by up to 22%.

Figures 1 and 2 show our results for water vapor in terms of precipitable water column for comparison with orbital data sets, and in terms of column-averaged volume mixing ratio for comparison with MSL's Rover Environmental Monitoring Station humidity sensor (REMS-H) measurements [10], respectively. In both figures the ChemCam measurements are shown in black points with 1-σ errors bars. Also shown in both figures is a red line that is a representation of the CRISM-derived Gale-localized water vapor retrievals from Toigo et al. [11]. This line is their Fourier-analysis-based fit shown in their figure 15 (re-scaled to appropriate units of each figure) and contains only annual and semi-annual components. It was derived from data points spanning MY 28 through early MY31 and is based on the statistics of individual ~20-meter-scale CRISM pixels (cf. [11] section 4.2.2) within a 136° – 140° East and 4° – 7° South box (A. Toigo, personal communication).

Comparison to orbital data sets. In Figure 1 we plot all Mars Years of the ChemCam water vapor on a single 0° – 360° x-axis and then add multiple versions of CRISM and Mars Global Surveyor (MGS) Thermal Emission Spectrometer (TES) water vapor

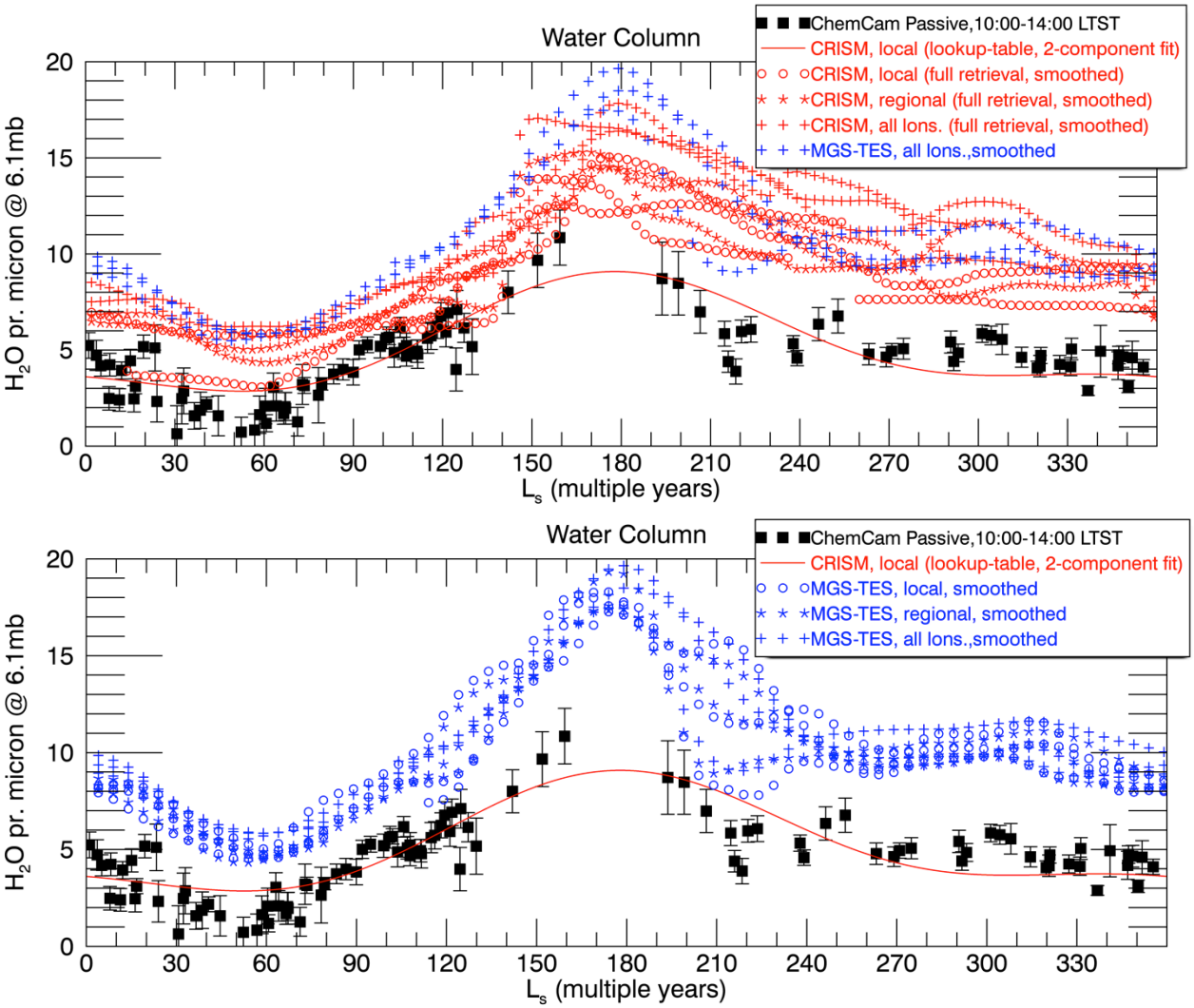

Figure 1: Water column from ChemCam passive sky (black squares) and from Toigo et al.'s [11] two-component fit to Gale-crater-localized CRISM lookup-table-based retrievals (red line) compared with various representations of CRISM and TES data sets. The details of these data sets are described in the text. All Mars years are plotted on the same x-axis. The ChemCam data plotted here is limited to results from 10:00 to 14:00 LTST. Water column is scaled to a 6.1 mb surface pressure. The two panels are identical except that some data sets are omitted from each panel for clarity.

column abundance data sets. The precipitable water column for all data sets in this figure is scaled to a 6.1 mb surface pressure. The TES data are the retrievals presented by Smith [12,13] except that they are the reprocessed version of those retrievals, which have updated H_2O-in-CO_2 line-broadening coefficients and which have been used in more recent inter-dataset comparisons such as Maltagliati et al. [14]. The CRISM data include results from the original CRISM "full" retrieval of Smith et al. [15] in addition to the Toigo et al. [11] two-Fourier-component fit. For both TES and the CRISM full retrieval we have smoothed the data sets with a 20° of L_s FWHM Gaussian-weighted moving average. For the CRISM retrievals we use only the first three Martian years of data because data points become relatively sparse after that. For purposes of comparison we define the "local" area of Gale crater to be the same latitude-longitude box used for the Toigo et al. [11] results. We also define a Gale crater "region" as 120° – 160° East, 0° to 10° South, and an "all longitudes" zonal-average as 0° – 360° East, 0° to 10° South.

It may seem surprising that the Smith et al. [15] "full" retrieval CRISM results and the Toigo et al. [11] lookup-table-based CRISM results are substantially different. However the former data set is limited by a small sample size at the "local" scale because it consists of only one retrieval per CRISM image – from a 2x2km central region in each image [15]. Meanwhile the lookup retrieval approach of the latter data set provides computationally efficient retrievals of individual pixels but it can be modestly biased relative to the "full" retrieval on which it is based [11]. We believe that a combination of such a bias with a small-number-statistics effect can explain the CRISM results discrepancies, but clearly further CRISM data analysis is needed to take full advantage of ChemCam vs. CRISM water vapor comparisons. Pending such analysis it does appear that the local CRISM data is a fairly close match to the ChemCam results in both magnitude and overall seasonal pattern. Interestingly, MGS-TES data localized to Gale Crater shows substantially more water vapor than does ChemCam or (apparently) CRISM, but is well matched to CRISM at regional and zonal scales.

The ChemCam water vapor abundances show one peculiar seasonal feature that is not present in any of the orbital data sets, that being a distinct minimum period between L_s = 30° and L_s = 70° where the scaled-to-6.1 mb column abundances is in the 1 – 2 precipitable micron range. A similar minimum *is* however present in upward-looking MER mini-TES water vapor retrievals [16].

Comparison with REMS-H. Figure 2 shows the full ~1.5 Martian Year span of the ChemCam data set in time order. For ChemCam and CRISM data on this plot, the column-averaged volume mixing ratio is found by simply dividing the mass of water vapor in the column (based on the retrieved value of precipitable microns) by the total atmospheric column mass (based on the REMS-measured surface pressure [17]) to find the column mass mixing ratio, and then multiplying by the ratio of molecular weights (=2.40) to give the volume mixing ratio. The column-averaged volume mixing ratio, in units of ppm, is thus related to the scaled-to-6.1-mb water column abundance, in units precipitable microns, by a constant factor of 14.54. (For mass mixing ratio the corresponding factor is 6.0.)

For Figure 2 the REMS-H relative humidity (RH) values are converted to mass mixing ratio using the saturation vapor pressure over ice at the REMS-H inlet temperature as described by Savijärvi et al. [18] and Martínez et al. [19], and then to volume mixing

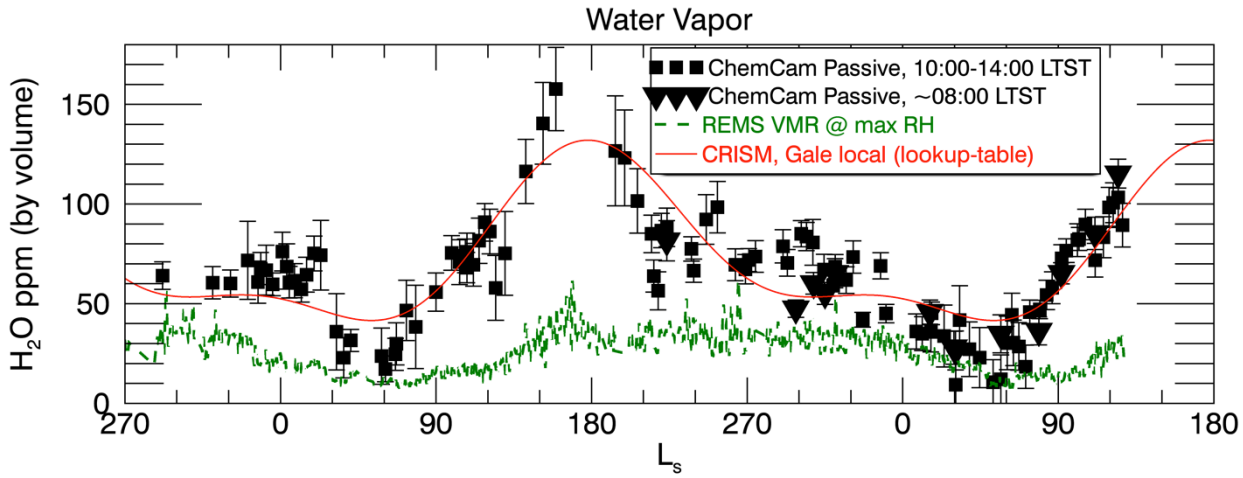

Figure 2: Column-averaged volume mixing ratios from: ChemCam passive sky (black squares and triangles); Toigo et al.'s [11] two-component fit to Gale-crater-localized CRISM lookup-table-based retrievals (red line). The x-axis begins in Mars Year 31 and continues into Mars Year 33. Also plotted is the REMS-H-derived *in-situ* volume mixing ratio at the time of maximum relative humidity on each sol (dashed green line), which always occurs in the early morning before sunrise. Note that this REMS-H value cannot be directly compared to the other quantities plotted here because it has not been measured during daylight hours.

ratio using the ratio of molecular weights. The REMS-derived mixing ratios are not available during daytime hours because the RH is too low for reliable measurements, but during the evening and nighttime hours REMS-H mixing ratios are typically observed to decrease as the night progresses until a mixing ratio minimum and relative humidity maximum is reached in the pre-dawn period [18, 20]. We take the approach of Martínez et al. [19,21] and use the mixing ratio at the time of maximum relative humidity, which is the most precise and reliable value and which corresponds to the pre-dawn mixing ratio minimum. In fact the REMS data that we show in Figure 2 is identical to figure 8 of Martinez et al. [19] except for REMS data set updates and the conversion from mass to volume mixing ratio. As described in Martinez et al. [19], among the full set of REMS-H measurements, only those taken during the first four seconds of measurements after the relative-humidity sensor has been turned on after ~5 min or more of inactivity are reliable. This is because heating of the sensor by the REMS control electronics causes an artificial decrease in the relative humidity values after the first four seconds of operations.

The in-situ REMS-H volume mixing ratios in Figure 2 cannot be directly compared to the ChemCam column-averaged volume mixing ratios because they are not available during daylight hours. Thus these comparisons are not intended as a simple cross-validation exercise – they are intended to address the physics controlling the water vapor vertical profile and its diurnal evolution [cf. 18,20]. What Figure 2 shows is that the pre-dawn (maximum RH) in-situ mixing ratios are in all seasons consistently lower that the column-averaged mixing ratio by a large factor, which ranges from ~1.4 to slightly larger than 5. Pending further analysis of REMS-H volume mixing ratio uncertainties, the differences between ChemCam and REMS-H pre-dawn mixing ratios appear to be much too large to be explained by large scale circulations, which supports the hypothesis of substantial diurnal interactions of water vapor with the surface as proposed by Jakosky et al. [22] and Savijärvi et al. [20]. We see no evidence of diurnal changes in the ChemCam water vapor data, but this is consistent with the Savijärvi et al. [20] prediction that only a very shallow layer of the atmosphere participates in the diurnal response.

Aerosol Results: Our aerosol retrievals should be considered preliminary but they yield mostly-reliable results for the dust and water ice aerosol contributions to column opacity and partially reliable results for dust aerosol particle size and for parameterized aerosol vertical profiles.

The most striking and apparently robust aerosol result is a two-fold increase in water ice aerosol opacity in the second year of ChemCam passive sky observations. We see no evidence for systematic errors that could produce such a change, but we are also not aware of any prior observations or models that suggest the possibility of interannual water ice aerosol changes of this magnitude. Clearly it will be important to seek confirmation of this result in other data sets.

For dust aerosol particle size, we see a strong and smoothly varying seasonal pattern that is consistent with Clancy et al.'s [23] MGS-TES emission-phase-function (EPF) results. The ChemCam particle sizes, unlike those derived from TES EPFs, show very little scatter about the smooth seasonal trend, perhaps because they cover only a single location.

For the aerosol vertical profiles we consistently find more low-level aerosol than expected from TES climatology and from Mars Climate Sounder vertical profiles. In fact mixing ratios are indicated to be consistently larger in the bottom scale height than at ~20km, which seems to contradict the Heavens et al. [24] observations of a "high-altitude tropical dust maximum". ChemCam is most likely more sensitive to the bottom scale height of aerosols than the MCS and TES limb-sounding retrievals, but given the preliminary nature of ChemCam aerosol results it is too early to say which instrument is providing the most accurate profile.

References: [1] Wiens et al. (2012) Space Science Reviews 170, 167-227. [2] Maurice et al. (2012) Space Science Reviews 170, 95-166. [3] Wiens et al. (2015) Elements 11, 33-38. [4] Maurice et al. (2016) Journal of Analytical Atomic Spectroscopy, 31:863-889. [5] Le Mouélic et al. (2015) Icarus 249, 93-107. [6] Johnson et al. (2015) Icarus, 249:74-92. [7] McConnochie et al. (2014) Eighth International Conference on Mars, abstract #1328. [8] McConnochie et al. (2015) AGU Fall Meeting, abstract #P22A-08. [9] Mahaffy et al. (2013) *Science*, *341*(6), 263–266. [10] Harri et al. (2014) J. Geophys. Res. (Planets) 119, 2132-2147. [11] Toigo et al. (2013) J. Geophys. Res. (Planets) 118, 89. [12] Smith (2002) J. Geophys. Res. (Planets) 107, 5115-1. [13] Smith (2004) Icarus 167, 148–165. [14] Maltagliati et al. (2011) Icarus 213, 480. [15] Smith et al. (2009) J. Geophys. Res, 114, E00D03. [16] Smith et al. (2006) J. Geophys. Res. (Planets) 111, E12S13. [17] Harri et al. (2014) J. Geophys. Res. (Planets), 119, 82–92. [18] Savijärvi et al. (2015) J. Geophys. Res. Planets, 120. [19] Martínez et al. (2016) Icarus 280, 93-102. [20] Savijärvi et al. (2016) Icarus 265, 63–69. [21] Martínez et al. (2016) LPSC 47, #1761. [22] Jakosky et al. (1997) Icarus 130, 87-95. [23] Clancy et al. (2003) J. Geophys. Res. (Planets) 108, 5098. [24] Heavens et al. (2011) J. Geophys. Res. (Planets) 116, E01007.